Microfluidic Manufacturing of SN-38-Loaded Polymer Nanoparticles with Shear Processing Control of Drug Delivery Properties

Yimeng Cao, Lisa Silverman, Changhai Lu, Rebecca Hof, Jeremy E. Wulff, & Matthew G. Moffitt

November 2019

Microfluidic Manufacturing of SN-38-Loaded Polymer Nanoparticles with Shear Processing Control of Drug Delivery Properties

Yimeng Cao; Lisa Silverman; Changhai Lu; Rebecca Hof; Jeremy E. Wulff and Matthew G. Moffitt*

Department of Chemistry, University of Victoria, P.O. Box 3065, Victoria, BC, Canada V8W 3V6

Abstract

Two-phase gas-liquid microfluidic reactors provide shear processing control of SN-38-loaded polymer nanoparticles (SN-38-PNPs). We prepare SN-38-PNPs from the block copolymer poly(methyl caprolactone-*co*-caprolactone)-*block*-poly(ethylene oxides) (P(MCL-*co*-CL)-*b*-PEO) using bulk and microfluidic methods and at different drug-to-polymer loading ratios and on-chip flow rates. We show that as the microfluidic flow rate (Q) increases, encapsulation efficiency and drug loading increase and release half times increase. Slower SN-38 release is obtained at the highest Q value (Q = 400 μL/min) than is achieved using a conventional bulk preparation method. For all SN-38-PNP formulations, we find a dominant population (by number) of nanosized particles (< 50 nm) along with a small number of larger aggregates (> 100 nm). As Q increases, the size of aggregates decreases through a minimum and then increases, attributed to a flow-variable competition of shear-induced particle breakup and shear-induced particle coalescence. IC_{25} and IC_{50} values of the various SN-38-PNPs against MCF-7 cells show strong flow rate dependencies that mirror trends in particle size. SN-38-PNPs manufactured on-chip at intermediate flow rates show both minimum particle sizes and maximum potencies with a significantly lower IC_{25} value than the bulk-prepared sample. Compared to conventional bulk methods, microfluidic shear processing in two-phase reactors provides controlled manufacturing routes for optimizing and improving the properties of SN-38 nanomedicines.

Keywords: drug delivery, microfluidics, polymer nanoparticles, SN-38

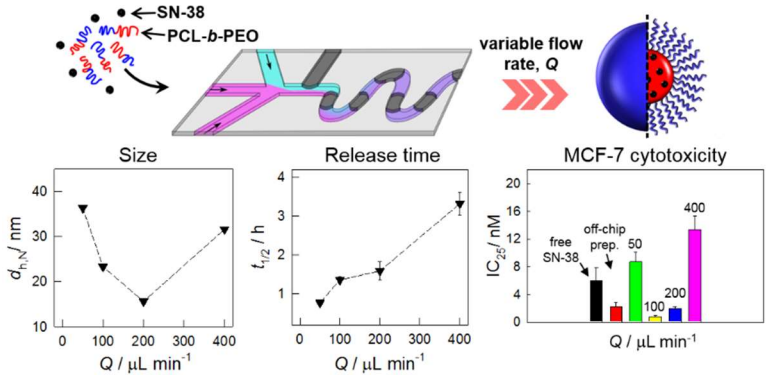

Introduction

The anticancer agent 7-ethyl-10-hydroxycamptothecin (SN-38) has shown promising *in vitro* potency against a wide range of tumor cells, including colorectal, breast, ovarian, and brain cancer, due to its activity as a DNA topoisomerase I inhibitor. SN-38 is the active metabolite of the commercially available prodrug irinotecan (Captosar®, Pfizer), although it is up to 1000× more potent than the prodrug due to poor conversion efficiencies of irinotecan in cancer patients.[1] However, the direct clinical use of SN-38 is hindered by its low water solubility leading to poor bioavailability *in vivo*. Another impediment to the effective administration of SN-38 is the poor stability of its active lactone form, which undergoes fast conversion to an inactive carboxylate form at physiological temperature and pH.[1, 2]

The above limitations of SN-38 delivery can be mitigated by encapsulation of the drug within various nanoparticle formulations,[2] including lipids,[3, 4] gold nanoparticles,[5] star polymers,[6, 7] and micellar polymer nanoparticles (PNPs).[1, 8-17] SN-38-loaded PNPs (SN-38-PNPs) formed from self-assembled amphiphilic block copolymers are the most widely studied drug delivery system for SN-38, due to advantages of stability and chemical functionalizability.[9] One SN-38 formulation, NK012, consisting of micellar PNPs of SN-38-conjugated poly(glutamic acid)-*block*-poly(ethylene oxide) (PGA-*b*-PEO), has completed phase II clinical trials, showing promising *in vivo* efficacy against various cancers and selective accumulation in tumours attributed to the enhanced permeability and retention (EPR) effect.[8-10] Other SN-38-PNP systems have incorporated added functionality *via* specific synthetic design or modification of the constituent block copolymer, including chemical responsivity,[11] active targeting,[1] combination therapy,[6] and theranostics.[13] SN-38-PNPs are typically manufactured using conventional self-assembly approaches, including nanoprecipitation,[1, 12-14, 16] thin film hydration,[15, 17] or dialysis.[11] In these

methods, PNP size, structure, and drug delivery properties are directed by intermolecular forces alone, which can be modulated only by changing the temperature or the chemistry of the formulation. New manufacturing methods for SN-38-PNPs that impart variable external mechanical forces to manipulate important figures of merit, including drug loading, release rates, and anticancer potency, without the need to change the polymer composition, polymer concentration, drug-to-polymer ratio, or solvent, could greatly enhance capabilities for optimizing SN-38 chemotherapy.

Our group has applied a two-phase, gas-liquid microfluidic platform for the manufacturing of PNP nanomaterials of controlled structure and properties.[18-30] In this reactor, counter-rotating vortices within the segmented liquid plugs enable fast on-chip mixing which triggers self-assembly and PNP formation.[18, 19] Subsequent downstream processing of the resulting PNPs occurs in high-shear "hot spots" as the formulation continues to move through the microchannels, analogous to industrial processing to modify the structure and properties of commodity polymer materials.[18, 19, 29] Using our microfluidic platform for producing PNP delivery vehicles for the common anticancer drug paclitaxel (PAX),[24, 26, 27, 30] we have shown that variation in the on-chip flow rate (which varies the maximum shear rate within the hot spots) provides a unique control handle on PNP sizes, morphologies, drug loading, release rates, and *in vitro* antiproliferation effects, independent of the formulation chemistry.

In this paper, we prepare SN-38-PNPs from a poly(methyl caprolactone-*co*-caprolactone)-*block*-poly(ethylene oxides) (P(MCL-*co*-CL)-*b*-PEO) block copolymer using bulk and microfluidic methods and at different drug-to-polymer loading ratios and on-chip flow rates. The mean sizes and size distributions of the resulting SN-38-PNPs are characterized using a combination of transmission electron microscopy (TEM) and dynamic light scattering (DLS), and

SN-38 encapsulation efficiencies (*EE*), drug loading (*DL*), and release rates are determined using high performance liquid chromatography (HPLC). Finally, *in vitro* cytotoxicity experiments are carried out to investigate the potency of the various SN-38 formulations against the human breast cancer cell line MCF-7. While *EE* and *DL* values do not change significantly with increasing microfluidic flow rate, *Q*, SN-38 release half times are shown to increase monotonically with increasing *Q*. Mean sizes of SN-38-PNPs are also found to be strongly dependent on microfluidic processing, first decreasing and then increasing with increasing manufacturing flow rate. Finally, we show that two-phase microfluidic SN-38 encapsulation significantly increases the potency of SN-38 against MCF-7 cells: intermediate microfluidic flow rates produce SN-38-PNPs that are more potent than those formed at extreme flow rates, and also more potent than those prepared using the conventional bulk method. These results underline the strong potential of on-chip shear processing for the manufacture and optimization of SN-38-containing nanomedicines for cancer treatment. In addition, comparison of these results with our previous study on microfluidic encapsulation of PAX in the same copolymer[30] reveals the generality of the shear processing strategy, while also emphasizing the important role of the nature of the drug in determining the specific structure and properties of drug delivery systems, even in the presence of strong processing forces.

Experimental

Materials. The block copolymer PMCL-25 was synthesized and characterized in our lab, as described in detail in a recent publication.[30] Briefly, PMCL-25 is a poly(methyl caprolactone-*co*-caprolactone)-*block*-poly(ethylene oxide) (P(MCL-*co*-CL)$_{5k}$-*b*-PEO$_{5k}$, $Đ$ = 2.55) block copolymer in which the hydrophobic core-forming block is a random copolymer consisting of 25 wt % MLC and 75 wt % CL monomers, and the subscripts refer to the number-average molecular

weights of the corresponding blocks. The MLC monomer is added to reduce the crystallinity of the hydrophobic block relative to the pure PCL polymer. We note that the relatively high dispersity of the block copolymer ($Đ$ = 2.55) does not preclude the formation of uniform PNPs; in our previous publication,[30a] we showed that PMCL-25 self-assembly *via* the bulk method (in the absence of drug) formed mainly uniform spheres with mean core diameter 22 ± 2 nm along with some short cylinders of mean width 17 ± 2 nm.

7-Ethyl-10-hydroxycamptothecin (SN-38) was purchased from AK Scientific (≥ 98.0%). NaCl (Bio Basic Canada, 99.9%), KCl (Caledon, 99.0%), Na_2HPO_4 (BioBasic Canada, 98.0%) and KH_2PO_4 (Caledon, 99.0%) were used to prepare phosphate buffered saline (PBS, pH = 7.4). *N*,*N*-dimethylformamide (DMF, Caledon, 99.8%), acetonitrile (Caledon, HPLC grade), and 1,1′-dioctadecyl-3,3,3′,3′-tetramethylindocarbocyanine perchlorate (DiI) (Aldrich) were used as received.

Bulk Preparation of SN-38-PNPs. PNPs containing various quantities of SN-38 were prepared by the nanoprecipitation method. Specifically, ~3 g of 0.33 wt % copolymer solutions in DMF containing three different drug-to-polymer ratios (w/w), r (r = 0.25, 0.50 and 0.75) were prepared and stirred overnight. Each solution was then added dropwise at a rate of 120 µL/min using a syringe pump into a 10× excess volume of deionized water with continuous high-speed stirring. In order to remove residual DMF, the resulting PNP dispersion was then dialyzed against deionized water for 12 hours with changing of water every hour for the first 4 h (6-8 kD MWCO dialysis membrane, Spectrum Laboratories). Precipitated drug in the aqueous dispersion was removed by centrifugation at 16000×g for 18 minutes; the resulting supernatant containing PNP-encapsulated SN-38 was decanted into a pre-weighed vial. Deionized water was added to the centrifuge tube in order to rinse the residue and minimize loss of any SN-38-PNPs trapped in the

pellet. Vortexing was applied for 5 min to the centrifugation tube in order to break up and re-suspend the pellet followed by another centrifugation step and collection of the supernatant. This rinsing process was repeated an additional two times.

Microfluidic Reactor Fabrication. Negative masters were fabricated on silicon wafers (Silicon Materials) using the negative photoresist SU-8 100 (Microchem). A 150 µm-thick SU-8 film was spin-coated at 2000 rpm onto the silicon wafer and heated at 65 °C for 12 min and then at 95 °C for 50 min. After the wafer was cooled, a photomask was placed directly above and the wafer was exposed to UV light for 100 s. Then, the UV-treated film was heated at 65 °C for 1 min and then 95 °C for 20 min. Finally, the silicon wafer was submerged in SU-8 developer (Microchem) and rinsed with isopropanol until all unexposed photoresist was removed.

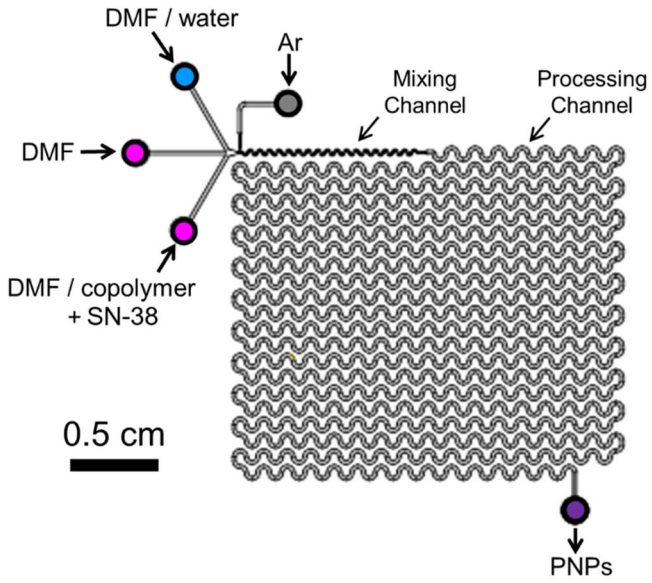

Figure 1. Schematic showing the two-phase gas-liquid microfluidic reactor used in this study.

Microfluidics chips were fabricated from poly(dimethyl siloxane) (PDMS) using a SYLGARD 184 silicon elastomer kit (Dow Corning). For fabrication of all PDMS chips, the elastomer and curing agent were mixed at a 7:1 ratio and degassed under vacuum. The resulting mixture was poured over a clean negative master chip in a Petri dish and further degassed until all remaining air bubbles were removed. The PDMS was heated at 85 °C until cured (~20 min), and then peeled from the negative master; holes were punched through the reservoirs of the resulting PDMS chip to allow for the insertion of tubing. A thin PDMS film (substrate layer) was also made on a glass slide by spin-coating a 20:1 elastomer / curing agent mixture followed by curing. The substrate layer was then permanently bonded to the base of the microfluidic reactor (channel layer) after both components were exposed to oxygen plasma for 45 s. The resulting reactor (Figure 1) has a set channel depth of 150 μm and consists of a sinusoidal mixing channel 100 μm wide and a sinusoidal processing channel 200 μm wide, identical to the reactor described in previous publications from our group.[24-30]

Flow Delivery and Control. Pressure-driven flow of liquids to the reactor inlet was provided using 1 mL gastight syringes (Hamilton, Reno, NV) mounted on syringe pumps (Harvard Apparatus, Holliston, MA). The microfluidic chip was connected to the liquid syringes *via* 1/16th-inch (OD) Teflon tubing (Scientific Products and Equipment, ON). Argon (Ar) gas flow was introduced to the chip *via* an Ar tank regulator and a downstream regulator (Johnston Controls) for fine adjustments. The chip was connected to the downstream regulator through a 1/16th-inch (OD) / 100-μm (ID) Teflon tube (Upchurch Scientific, Oak Harbor, WA). The liquid flow rate (Q_{liq}) was programmed *via* the syringe pumps and the gas flow rate (Q_{gas}) was fine-tuned *via* the downstream pressure regulator in order to set the nominal total flow rates (Q) of 50, 100, 200 and 400 μL/min described in the main text. Due to the compressible nature of the gas and the high

gas/liquid interfacial tension, discrepancies arise between the nominal (programmed) and actual values of Q_{gas}, Q_{gas}/Q_{liq}, and the total flow rate (Q_{total}). Therefore, actual values of Q_{gas}, Q_{gas}/Q_{liq} and $Q_{total} = Q_{gas} + Q_{liq}$ for each microfluidic experiment (*Supporting Information*, Table S1) were calculated from the frequency of bubble formation and the average volume of gas bubbles, determined from image analysis of the mean lengths of liquid and gas plugs, L_{liq} and L_{gas}, respectively, under a given set of flow conditions. This method of flow calculation has been previously described by our group.[19] For all experiments, the relative gas-to-liquid flow ratio, Q_{gas}/Q_{liq} ~1 and all actual Q_{total} values are within 10% of nominal Q values reported in the main text.

Visualization of the gas bubbles and liquid plugs within the microfluidic reactor was achieved using an upright optical microscope (Omax) with a 10× objective lens. Images were captured using a 2.07 megapixel PupilCam camera (Ken-A-Vision) and mean lengths of liquid and gas plugs were determined from the images using image analysis software (ImageJ).

Microfluidic Preparation of SN-38-PNPs. For microfluidic preparation of SN-38-PNPs, the following three fluid streams were combined to form gas-segmented liquid plugs within the reactor: (1) 1.0 wt % PMCL-25 solution in DMF with SN-38/polymer (w/w) loading ratios of r = 0.25, 0.50 and 0.75 (2) pure DMF, and (3) DMF/water. The flow rates of the three liquid streams were equal for all runs and the water content of the DMF/water stream was selected to yield steady state on-chip concentrations of 0.33 wt % copolymer and 13.6 wt % water. The critical water content of 0.33 wt % PMCL-25 in DMF was previously determined to be 8.6 wt %,[30] so that the water content for microfluidic SN-38-PNP preparation is designated cwc + 5 wt %.

For each SN-38-PNP preparation, the sample was collected from the chip into vials containing 10× excess by volume of deionized water. In order to remove residual DMF, the

resulting PNP dispersion was then dialyzed against deionized water for 12 hours with changing of water every hour for the first 4 h (6-8 kD MWCO dialysis membrane, Spectrum Laboratories). Precipitated drug in the aqueous dispersion was removed by centrifugation at 16000×g for 18 minutes; the resulting supernatant containing PNP-encapsulated SN-38 was decanted into a pre-weighed vial. Deionized water was added to the centrifuge tube in order to rinse the residue and minimize loss of any SN-38-PNPs trapped in the pellet. Vortexing was applied for 5 min to the centrifugation tube in order to break up and re-suspend the pellet followed by another centrifugation step and collection of the supernatant. This rinsing process was repeated an additional two times.

Transmission Electron Microscopy. Negatively-stained samples for transmission electron microscopy (TEM) imaging were prepared by depositing a drop of SN-38-PNP dispersion on a carbon-coated 300-mesh copper TEM grid followed by a drop of 1 wt % uranyl acetate aqueous solution as a negative staining agent. Excess liquid was immediately removed using lens paper, followed by drying of the remaining liquid under ambient conditions. Imaging was performed on a JEOL JEM-1400 transmission electron microscope, operating at an accelerating voltage of 65 kV and equipped with a Gatan Orius SC1000 CCD camera. Mean core sizes were determined by averaging average core sizes from three separate images of different regions of the TEM grid (N > 150 PNPs). Standard errors are reported to represent the precision of mean core sizes determined from triplicate images in different regions of the TEM grid. Standard error (SE) was calculated from the standard deviation (SD) of average core sizes from the three images: $SE = \frac{SD}{\sqrt{3}}$.

Dynamic Light Scattering. Effective hydrodynamic diameters and size distributions of SN-38-PNPs were determined using dynamic light scattering (DLS). DLS measurements were

carried out using a Brookhaven Instruments Zeta-Pals Analyzer equipped with a solid state Laser (660 nm) with a maximum power output of 35 mW. All DLS measurements of SN-38-PNPs were performed in pure water and an experimental temperature of 25˚C and at a scattering angle of 90˚. For each SN-38-PNP preparation, mean effective hydrodynamic diameters $d_{h,eff}$ were determined from three measurements of the autocorrelation function using cumulent analysis. Reported mean effective hydrodynamic diameters for each condition of r and Q were determined by averaging values from triplicate preparations. Standard errors are reported to represent the precision of mean hydrodynamic diameters determined from triplicate preparations. Standard error (*SE*) was calculated from the standard deviation (*SD*) of mean effective hydrodynamic diameters across the triplicate preparations: $SE = \frac{SD}{\sqrt{3}}$. For some SN-38-PNP samples, number-average hydrodynamic diameters $d_{h,N}$ are also reported and these values are determined from CONTIN number distributions.

SN-38 Encapsulation Efficiency Determination. High performance liquid chromatography (HPLC, Ultimate 3000, Thermo Scientific) equipped with a C18 column (Phenomenex Luna 5u C18) and a UV detector set at 265 nm was used to determine the drug loading efficiencies of SN-38-PNPs. The mobile phase, consisting of acetonitrile and water (65:35, v/v) was running at 1 ml/min. The mobile phase was adjusted to pH = 3 by formic acid to ensure SN-38 was in the closed lactone ring form during the assay. For each SN-38 sample, water was removed by rotary evaporation at 25 °C followed by addition of acetonitrile to dissolve the solid. 50 μL of the resulting solution was then injected into the instrument and the UV detector reading of SN-38 in the sample was recorded. A calibration curve was made by analysis of 5 standards consisting of known concentrations of SN-38 in acetonitrile (5, 10, 20, 50, 100 ppm). All HPLC measurements were carried out at 25 °C.

Quantities of SN-38 in the various dissolved SN-38-PNP solutions were determined using the calibration curve. Encapsulation efficiencies (*EE*) and drug loadings (*DL*) were calculated for each sample using the following equations:

$$EE\ /\ \% = \frac{mass\ encapsulated\ SN-38}{total\ mass\ SN-38} \times 100$$

$$r = \frac{total\ mass\ SN-38}{mass\ copolymer}$$

$$DL\ /\ \% = \frac{mass\ encapsulated\ SN-38}{mass\ encapsulated\ SN-38 + mass\ copolymer} \times 100$$

$$DL\ /\ \% = \frac{r \times EE}{(r \times EE) + 1} \times 100$$

Reported *EE* and *DL* values for each condition of *r* and *Q* were determined by averaging values from triplicate preparations. Standard errors are reported to represent the precision of mean *EE* and *DL* values determined from triplicate preparations, with standard error (*SE*) calculated from the standard deviation (*SD*) across the triplicate preparations: $SE = \frac{SD}{\sqrt{3}}$.

***In Vitro* SN-38 Release Kinetics.** Experiments were carried out to monitor the *in vitro* release of SN-38 from SN-38-PNPs using HPLC. In a typical experiment, a known mass (~2 g) of SN-38-loaded nanoparticles were put into a 5 mL Float-A-Lyzer tube (SpectrumLabs, MWCO 100 kDa) for each predetermined release time (t = 1, 2, 4, 8, 12, 18, 24 h). These tubes were then placed in a 5 L-beaker of the release medium, consisting of ~4 L of PBS; throughout release experiments, the release medium was constantly stirred using magnetic stirring and maintained at physiological temperature (37 ± 0.2°C). At each predetermined time, one of the seven tubes was transferred to a vial and dried by rotary evaporation at 25 °C. Then a known quantity of acetonitrile was added to dissolve SN-38 and vortex was applied for 5 min to make sure all the SN-38 was dissolved. The

concentration of the resulting solution was measured by HPLC (see previous section for specifications). Percentages of SN-38 released were calculated relative to determined masses of SN-38 in PNPs at the $t = 0$ release time. Reported release percentages at each time are averages determined from triplicate preparations under the specified conditions. Standard errors are reported to represent the precision of mean release percentages determined from triplicate preparations, with standard error (*SE*) calculated from the standard deviation (*SD*) across the triplicate preparations: $SE = \frac{SD}{\sqrt{3}}$. The release profiles were fit using the Levenburg Marquardt algorithm within XLFit, an add-in for Microsoft Excel. The following fitting model was used for all conditions:

$$y = \left(\frac{1}{2B}\right)[x+A+B-((x+A+B)^2-(4xB)^{0.5}].$$

Mean release profiles and release half times were thus determined for microfluidic SN-38-PNPs prepared at various flow rates. Since the objective of these experiments was to investigate the effect of shear processing on SN-38 release times, water-dispersible, bulk-prepared SN-38-PNPs formed in the absence of high shear served as an appropriate control.

Cell-Culture and Antiproliferation Assay. MCF-7 cells were grown to ~80% confluence in Dulbecco's Modified Eagle's Medium (DMEM) supplemented with 10% fetal bovine serum (FBS) in a 75 cm^2 tissue culture flask and maintained at 37 °C with 5% CO_2 in a tissue culture incubator. Cells were then trypsinized, collected and pelleted by centrifugation at 4 ºC and 1200 rpm for 5 minutes. The cell pellet was then resuspended in DMEM media and the cell concentration was determined using a hemocytometer. After the initial cell concentration was determined the suspension was diluted to 1.0×10^5 cells/mL. Next, a multichannel pipet was used to fill a 96 well plate with 100 µL/well of the diluted cell suspension. The cell loaded plates were then incubated for 24 h at 37 °C under an atmosphere of 5% CO_2.

After 24 hours cell incubation, 6.5 µL aliquots of stock SN-38-PNP dispersions or 6.5 µL of free SN-38 dissolved in dimethylsulfoxide (DMSO) were diluted to a total volume of 650 µL with DMEM media. Serial dilutions were carried out, and then 100 µL of each diluted stock was added to the appropriate well of the 96-well plate (containing ~1.0×10^4 cells in 100 µL of media, as described above), in order to generate a range of different concentrations for analysis. The treated cells were incubated for 48, 72 or 96 hours at 37 °C under a 5% CO_2 atmosphere. In order to determine cell viability, 20 µL of CellTiter-Blue was added to each well after the predetermined incubation time was complete. After the addition of the CellTiter-Blue the 96 well plates were incubated for 4 hours (5% CO_2, 37 °C) and then fluorescence (λ_{ex} = 560 nm; λ_{em} = 590 nm emission) readings were recorded on a 96-well plate reader. Cell death was calculated for each well, based upon the following formula:

$$\%\, Death = \left[1 - \frac{(S - B_o)}{(B_t - B_o)}\right] \times 100$$

where S is the sample reading (cells + drug + media), B_t is the average reading for the untreated population of cells (cells + media), and B_0 is the average reading of wells containing media only (media). *% Death* vs. SN-38 concentration data sets, which combined data from three separate SN-38 preparations for each condition, were fit using XLfit (IDBS). IC_{25} and IC_{50} values were then determined by calculating the SN-38 concentration required to elicit a 25% or 50% reduction in cell viability, respectively, based on the fitted curves. Experimental error on these values was determined based on the quality of the fits.

Fluorescence Imaging of PNP Cell Uptake. PNPs labeled with the fluorescent dye DiI were prepared using identical microfluidic conditions to those described previously (Q = 200 µL/min), except with DiI in place of SN-38 (r = 0.5). For cell imaging, MCF-7 cells were seeded

at a density of 10^4 cells per well in a 96 well plate, and allowed to incubate in 200 μL DMEM (containing 10% FBS) overnight. The DiI-labeled PNP suspension was mixed 1:1 with cell media (DMEM containing 10% FBS), for a final copolymer concentration of approximately 0.15 mg/mL. After overnight incubation, cells were washed with 1×PBS and the media was replaced with 250 μL of the media/PNP mixture. Cells were incubated for 3 h then were washed twice with 1×PBS. 4′,6-Diamidino-2-phenylindole (DAPI, Life Technologies Corporation) was dissolved at a concentration of 1 μg/mL in DMSO, and further diluted 10-fold in PBS buffer, to afford a final concentration of 0.1 μg/mL. 50 μL was added to each well and cells were incubated on the benchtop for 5 min then washed twice with cold PBS buffer. Fluorescein diacetate (Sigma F-7838F7378) was dissolved at a concentration of 5 mg/mL in DMSO, and then serially diluted 100-fold and then 50-fold in PBS buffer, to afford a final concentration of 1 μg/mL. 100 μL was added per well and cells were incubated on the benchtop for an additional 5 min, and then washed twice with cold PBS buffer and immediately imaged. Cells were imaged using a Cytation5 fluorescent microscope plate reader, with three fluorescent filter cubes of emission (nm) / excitation (nm) = 377/447, 469/525, and 586/647. Images were taken using both 20× and 60× objectives.

Statistics and Data Handling. For comparison of cytotoxicity data (Figure 8), dose-response curves were first established as described in the section on Cell-Culture and Antiproliferation Assay. Serial dilutions provided samples of seven different concentrations for testing. Duplicate samples were either exact replicates (such that the same seven concentrations were tested in multiple wells) or shifted replicates (such that each series was shifted in concentration by an equivalent amount, relative to the same well of the starting series). Either way, the Excel application XLfit 5.5 (IDBS) was used to provide a best-fit curve of combined data of percentage cell death vs. concentration, together with IC_{25} and IC_{50} results and standard errors

derived from the goodness of fit. To compare any two results, the combined standard error SE_c was calculated from the square root of the sum of the squares of the standard errors from the individual curve fits:

$$SE_c = \sqrt{SE_1^2 + SE_2^2}$$

Similarly, the combined degrees of freedom *DOF* were calculated based upon the number of values (*N*) in each data set:

$$DOF = [(N_1 - 1) + (N_2 - 1)]$$

Regardless of whether exact replicates or shifted replicates were used, *N* was set to 7 for each experiment (the number of values per series). *DOF* was therefore equal to 12 for each pairwise comparison.

The difference between measured results (*t*) was then expressed in terms of units of combined standard error:

$$t = \frac{IC_1 - IC_2}{SE_c}$$

Finally, a *p* value was calculated using a two-tailed test. This was carried out with the TDIST function in Excel for all pairwise comparisons, using the equation:

$$p = \mathrm{TDIST}(t, DOF, 2)$$

For statistical comparisons where standard error could not be taken directly from a fitted curve, multiple measurements were carried out (at least three independent measurements per data point), and standard error was calculated as standard deviation across the measurements, divided by the square root of the number of samples:

$$SE = \frac{SD}{\sqrt{N}}$$

Two-tailed p-values were then calculated as above. In all cases, differences were assumed to be statistically significant when $p < 0.05$.

Results and Discussion

Encapsulation Efficiencies and Drug Loading Levels in SN-38-PNPs

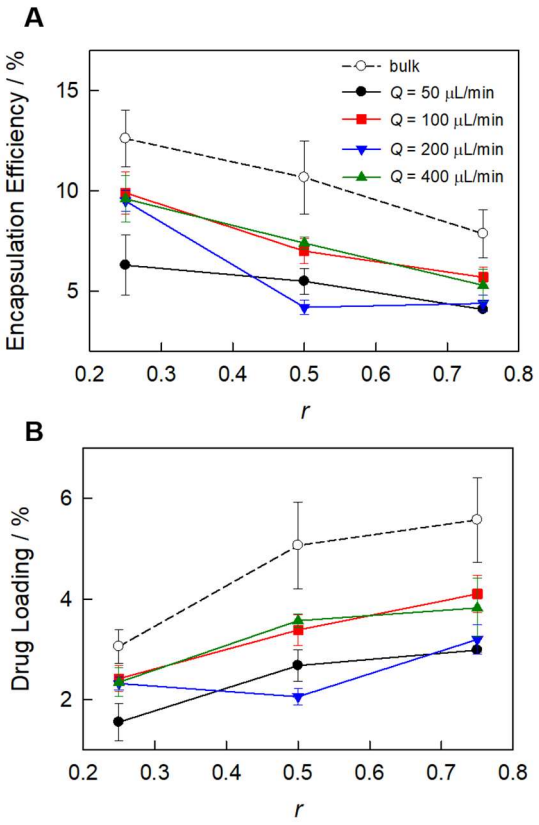

Figure 2. (A) Encapsulation efficiency (*EE*) and (B) drug loading (*DL*) plotted vs. loading ratio (*r*) for various bulk and microfluidic SN-38-PNP preparations.

Figure 2 shows plots of encapsulation efficiencies (*EE*, Figure 2A) and drug loading percentages (*DL*, Figure 2B) vs. SN-38/polymer (w/w) loading ratio, *r*, for various bulk and microfluidic preparations. For each data point, the experimental error (*SE*) was calculated from the standard deviation (*SD*) of three separate preparations under identical chemical and flow conditions, using:

$$SE = \frac{SD}{\sqrt{N}}$$

Therefore the reported error bars provide information on the reproducibility of a given manufacturing method and condition. In general, error bars are smaller for microfluidic preparations, indicating greater reproducibility than the bulk method. For example, the average relative error in *EE* for the bulk preparations (averaged over all *r* values) is 14.4% while those of the four microfluidic flow rates are 12.3%, 9.6%, 7.6%, and 10.4% for Q = 50, 100, 200, and 400 μL/min, respectively.

Although microfluidic effects (including fast mixing and high shear) improved reproducibility, they did not increase SN-38 loading efficiencies relative to conventional bulk PNP manufacturing. In fact, the current data showed that microfluidic preparations at various flow rates led to lower *EE* and *DL* values than the bulk method (Figure 2). It is important to note that for other chemical formulations previously self-assembled using the same microfluidic reactor, we have found microfluidic *EE* and *DL* values to be either higher or lower compared to bulk preparations, depending on the polymer, drug, and drug-to-polymer loading ratio.[24-27,30] In the current work, both bulk and microfluidic preparations show a trend of decreasing encapsulation efficiencies as the amount of added SN-38 increases (*EE* vs. *r*, Figure 2A), while the corresponding loading levels show a slightly increasing trend (*DL* vs. *r*, Figure 2B). These data suggest that as the relative amount of added SN-38 increases, a greater percentage of SN-38 remains unencapsulated, although the total amount of encapsulated material appears to increase, perhaps due to favourable mutual interactions between encapsulated SN-38 molecules. The maximum observed SN-38 loadings for both bulk and microfluidic preparations resulted from the r = 0.75 SN-38/polymer (w/w) loading ratio (*DL* = 5.6 % and 4.1 %, respectively). Such low loading levels are typical of SN-38 encapsulation in aliphatic polyester-based PNPs.[15]

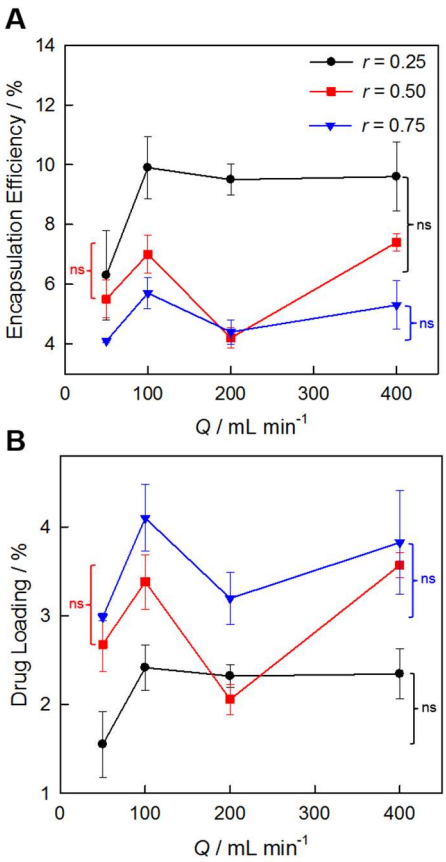

Figure 3. (A) Encapsulation efficiency (*EE*) and (B) drug loading (*DL*) plotted vs. manufacturing flow rate (*Q*) for various microfluidic SN-38-PNP preparations. Statistical comparisons between Q = 50 µL/min and Q = 400 µL/min data points (ns, $p > 0.05$) indicate no significant differences between *EE* and *DL* values obtained at the lowest and highest investigated flow rates.

For microfluidic preparations, the trends in encapsulation efficiency (*EE* vs. *Q*, Figure 3A) and drug loading (*DL* vs. *Q*, Figure 3B) with increasing flow rate are nonmonotonic but quite consistent for all three *r* values. For each drug-to-polymer ratio, mean values of *EE* and *DL* increase when the flow rate increases from Q = 50 µL/min to Q = 100 µL/min. This feature may be a result of improved SN-38 loading with concomitant improvements in mixing between copolymer and drug as the flow rate ramps up from its lowest value. Another consistent feature of the three plots are decreases followed by increases in *EE* and *DL* between Q = 100 µL/min and Q = 400 µL/min. It is noted that these dips in *EE* and *DL* correspond to minima in effective

hydrodynamic diameters, $d_{h,eff}$, from DLS (Figure 4A) as described in the following section. This correlation is understandable, since larger PNPs are better able to encapsulate SN-38 due to larger hydrophobic volume, as previously observed.[24, 31, 32] Despite the consistent trends for different *r* values in Figures 4A and 4B, statistical comparisons between data points show no significant changes in *EE* and *DL* with increasing flow rate between Q = 50 μL/min and Q = 400 μL/min. It is instructive to compare the observed trend in SN-38 *EE* values with flow rate (Figure 3A) with our earlier study of PAX encapsulation under identical conditions, which showed relatively constant *EE* values over the same range of flow rates.[30b] This difference highlights that while shear processing control in two-phase microfluidic reactors can be applied to multiple nanomedicine formulations, specific trends in PNP properties with respect to manufacturing flow rate can be strongly dependent on the choice of encapsulated drug.

Size and Size Distributions of SN-38-PNPs

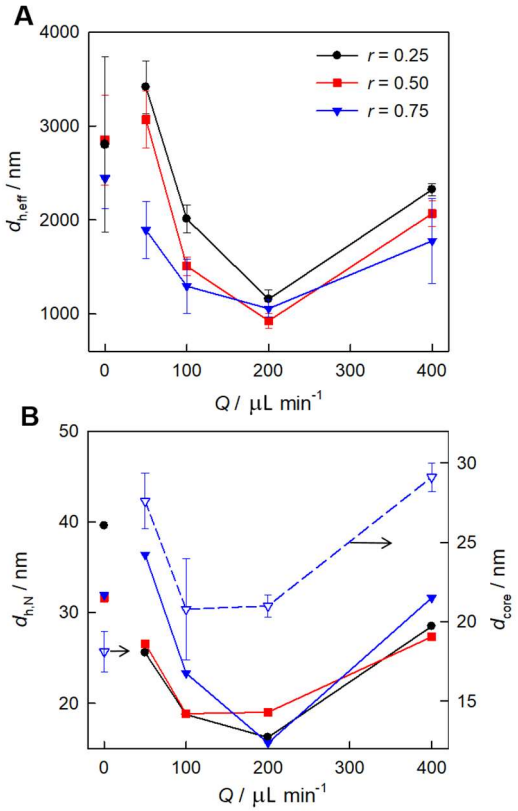

Figure 4. (A) Effective hydrodynamic diameters ($d_{h,eff}$) and (B) number-averaged hydrodynamic diameters ($d_{h,N}$) plotted vs. manufacturing flow rate (Q) for various SN-38-PNP preparations. The right-hand axis in (B) shows mean core diameters, d_{core}, for the small particle populations (< 100 nm) from TEM images. In (A) and (B), values for bulk-prepared PNPs are also shown (Q = 0) for comparison.

In this section we show significant effects of microfluidic processing on mean PNP sizes and size distributions. Figure 4A shows intensity-average mean effective hydrodynamic diameters, $d_{h,eff}$, of microfluidic-prepared SN-38-PNPs obtained from cumulent analysis of DLS autocorrelation functions plotted versus Q for the three SN-38/polymer (w/w) loading ratios of r = 0.25, 0.50, and 0.75. Values of $d_{h,eff}$, for bulk-prepared SN-38-PNPs (Q = 0 µL/min) are shown for comparison with microfluidic-prepared samples. For all three loading ratios, we find a general

trend of decreasing then increasing mean particle size as the manufacturing flow rate increases, with a common minimum mean particle size of ~1000 nm at Q = 200 µL/min. Bulk-prepared $d_{h,eff}$, values are found to be similar or higher than the highest on-chip values, obtained at the lowest microfluidic flow rate of Q = 50 µL/min. The large effective hydrodynamic diameters of both bulk and microfluidic samples suggest strong light scattering contributions from large aggregates. Therefore, a combination of CONTIN analysis of DLS data and TEM was applied to obtain a more complete picture of SN-38-PNP populations formed at various microfluidic flow rates.

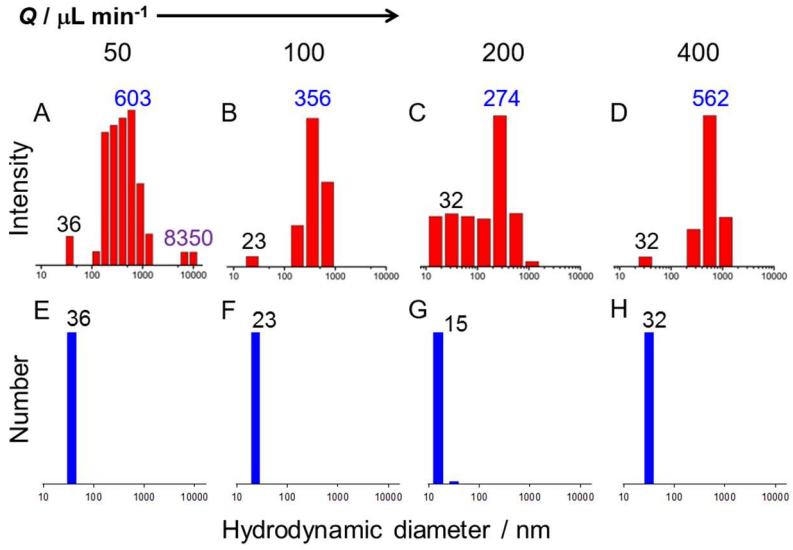

Figure 5. DLS data showing CONTIN intensity distributions (A-D) and number distributions (E-H) for microfluidic SN-38-PNPs prepared with various flow rates (Q) and r = 0.75.

For this analysis, we focus on the r = 0.75 SN-38/polymer (w/w) loading ratio, since these PNP samples were carried forward to *in vitro* experiments due to their higher *DL* values (Figure 3). CONTIN intensity distributions for SN-38-PNPs (which highlight large particles) prepared on-chip at four different flow rates and a SN-38/polymer (w/w) loading ratio of r = 0.75 are shown in Figure 5, A-D, revealing that relative intensities of large and small particle populations vary strongly with changing flow rate. At the lowest flow rate (Q = 50 µL/min), three separate

populations are identified (Figure 5A): small (< 100 nm), medium (100-1000 nm), and large (>1000 nm) particles, labeled according to the mode diameter in each population. When the flow rate increases to Q = 100 μL/min, the population of large particles disappears and the mode diameter of medium particles decreases (Figure 5B). When the flow rate further increases to Q = 200 μL/min, the relative intensity of small particles reaches a maximum and the mode diameter of medium particles further decreases (Figure 5C). Finally, a further increase in the flow rate to Q = 400 μL/min leads to a decrease in the relative intensity of small compared to medium particles along with an increase in the mode diameter of medium particles (Figure 5D).

Both the trends in $d_{h,eff}$ values from cumulant analysis (Figure 4A) and the changes in CONTIN intensity distributions (Figure 5, A-D) suggest competing effects of shear-induced particle breakup and shear-induced particle coalescence as the flow rate and maximum shear rate increase, as we have previously demonstrated in the gas-liquid microfluidic reactors.[19, 20, 23, 24, 27] Exposure to flow-variable high shear "hot spots" within the microchannels results in processing of polymer particles following initial self-assembly, leading to final particle populations that depend on both self-assembly conditions and subsequent on-chip processing.[20, 23, 24, 27] Bulk-prepared PNPs formed in the absence of shear processing show large $d_{h,eff}$ values (~2000-3000 nm), suggesting that large micron-scale aggregates are inherent to self-assembly for these mixtures of copolymer and SN-38. These large aggregates are sensitive to shear-induced particle breakup due to relatively high capillary numbers.[20, 23] Therefore when self-assembly occurs on-chip, subsequent shear processing within the "hot spots" effects a decrease in $d_{h,eff}$ with increasing on-chip flow rate (and maximum shear rate) between Q = 50 μL/min to Q = 200 μL/min, as the large and medium aggregates experience increasing shear-induced breakup into nanoscale PNPs (Figure 4A). This effect is also supported by the corresponding intensity distributions (Figure 5, A-C),

which show a decrease in relative intensity and mode size of large and medium aggregate populations, and an increase in the relative intensity of small particle populations, as the flow rate increases from Q = 50 μL/min to Q = 200 μL/min. A competing effect of shear is shear-induced coalescence of small particles into medium and larger aggregates.[20, 23] This effect will become increasingly important as the size and number of large particles sensitive to breakup decreases, leading to a minimum in $d_{h,eff}$ at Q = 200 μL/min and subsequent increase mean size as the flow rate continues to increase to Q = 400 μL/min. We also see the role of shear-induced coalescence in the intensity distributions (Figure 5, C and D), with the relative intensity of small particles decreasing and the mode size of medium particles increasing between Q = 200 μL/min to Q = 400 μL/min. The specific role of SN-38 in the observed size effects under shear processing (Figure 5A) is highlighted by comparison with previous results in which a different molecule, PAX, was encapsulated in the same copolymer under identical conditions of loading ratio (r = 0.25) and flow rates (Q = 50 μL/min to Q = 200 μL/min).[30] In the case of PAX, small, uniform spheres ($d_{h,eff}$ = 50-60 nm) were formed independent of flow conditions, with no discernable formation of larger aggregates.[30] This marked contrast in self-assembly behaviour is tentatively attributed to the relative conformational rigidity of SN-38 compared to PAX, leading to differences in core solubility and thus in the sizes and curvatures of the resulting aggregates, irrespective of equivalent shear forces acting on both systems.

It is important to note that both $d_{h,eff}$ values from cumulent analysis (Figure 4A) and CONTIN intensity distributions (Figure 5, A-D) are highly sensitive to the presence of strongly scattering medium and large aggregates within the sample, even though there are very few of these aggregates compared to small particles. Since it is the nanosized (<100 nm) particles that are important for therapeutic activity, it is therefore useful to apply analyses and methods that are

sensitive to these populations. CONTIN number distributions (which highlight small particles) for the four microfluidic samples are shown in Figure 5, E-H. Each of these distributions show dominant populations of small particles (d_h = 15-36 nm) formed at the various flow rates. In Figure 4B, number-average hydrodynamic diameters ($d_{h,N}$), which are sensitive to the more numerous small particles in the sample, are plotted versus Q for all three drug-to-polymer ratios. These plots show trends similar to those of $d_{h,eff}$ (Figure 4A), first decreasing then increasing as the flow rate increases. This indicates that the flow-modulated competition between shear-induced particle breakup and shear-induced particle coalescence, along with controlling the relative contribution of large aggregates (Figure 4A), also allows tuning of nanoscale PNPs within sample distributions (Figure 4B). Such nanoscale tuning of PNP sizes enables processing-based control of size-dependent nanomedicine properties, as demonstrated in a subsequent section.

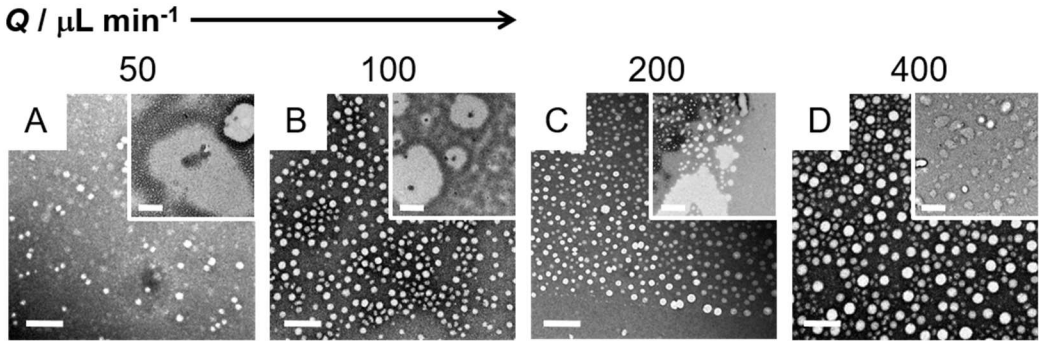

Figure 6. TEM images for microfluidic SN-38-PNPs prepared with various flow rates (Q) and r = 0.75. Main images show predominant populations of nanoscale (< 100 nm) PNPs and insets show low-magnification images of large aggregates. Scale bars are 200 nm and 500 nm in main images and insets, respectively.

Next, we applied TEM to visualize large and small particles, and to further quantify the small particle populations (< 100 nm). Figure 6 shows TEM images of SN-38-PNP samples associated with the CONTIN distributions in Figure 5. TEM of all four samples (r = 0.75, Q = 50,

100, 200, and 400 μL / min) reveals a predominant population of small spheres (< 100 nm) along with larger, irregular shaped aggregates up to several microns across (insets). Particle size analysis of the small spheres from TEM images yielded d_{core} values for each flow rate, which are plotted in Figure 4B for the r = 0.75 series (open blue triangles). These values are mostly consistent with associated $d_{h,N}$ values from DLS data (closed blue triangles), and follow the similar trend of decreasing then increasing PNP sizes attributed to the predominance of shear-induced particle breakup between Q = 50 μL/min and Q = 200 μL/min and shear-induced particle coalescence between Q = 200 μL/min and Q = 400 μL/min. For comparison with microfluidic-prepared PNPs, a representative TEM image and associated DLS data for bulk-prepared PNPs are presented in *Supporting Information* (Figure S1).

SN-38 Release Profiles from SN-38-PNPs. The *in vitro* SN-38 release kinetics were investigated for the series of bulk and microfluidic SN-38-PNP samples prepared with a SN-38/polymer (w/w) loading ratio of r = 0.75 and variable flow rates. We note that *in vitro* release rates are in general highly dependent on the specific conditions of the experiment,[25] so these conditions (temperature, release medium, membrane) were held constant for the current series of PNPs. Another important caveat for this discussion is that *in vitro* release kinetics are typically very different from *in vivo* pharmacokinetics due to the added complexities of living systems.[25, 33-35] However, the resulting release profiles provide important comparative information for future *in vivo* testing and clearly demonstrate the effect of microfluidic flow on release kinetics from SN-38-PNPs.

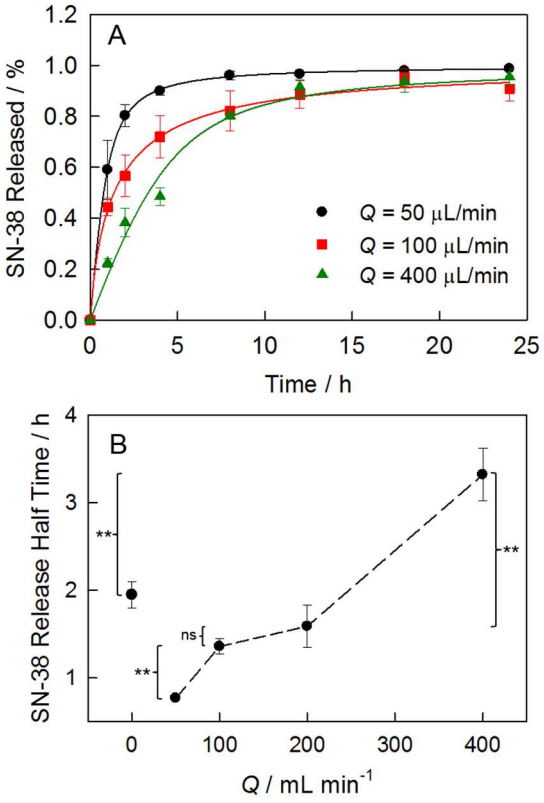

Figure 7. (A) Selected *in vitro* SN-38 release profiles and associated fits for microfluidic SN-38-PNPs prepared with various flow rates (Q) and $r = 0.75$. (B) Microfluidic SN-38 release half times determined from fits to release profiles plotted vs. manufacturing flow rate, Q; the release half time of bulk-prepared SN-38 PNPs is shown for comparison (Q = 0 µL/min). Statistical comparisons between $t_{1/2}$ values in (B) are indicated ** ($p < 0.005$), * ($p < 0.05$), or ns ($p > 0.05$).

Selected release profiles for SN-38-PNPs prepared at microfluidic flow rates of Q = 50 µL/min, Q = 100 µL/min, and Q = 400 µL/min, along with associated fits, are shown in Figure 7A. The three release profiles are clearly different and suggest slower SN-38 release with increasing microfluidic flow rate. For clarity, release profiles for bulk and Q = 200 µL/min are shown in *Supporting Information* (Figure S2). We quantified the effect of microfluidic flow rate on the release kinetics by determining release half times from the fits for all five release profiles in Figure 7A and Figure S2. SN-38 release half times are plotted with respect to Q in Figure 7B,

where Q = 0 μL/min represents the bulk condition. This plot shows a steady slowing of SN-38 release as the microfluidic flow rate increases. The release half-time of bulk-prepared SN-38-PNPs is an intermediate value that is significantly lower than that of the microfluidic sample prepared at the fastest flow rate (Q = 400 μL/min, Figure 7B), indicating that microfluidic manufacturing of SN-38-PNPs at high flow rate enables slower drug release than can be obtained by a conventional bulk preparation.

Unlike the sizes of SN-38-PNPs, which go through a minimum as the microfluidic flow rate increases (Figure 4), increases in SN-38 release half times are monotonic with increasing Q. This suggests that PNP core size is not a determining factor in flow-dependent changes to SN-38 release rates. We have previously shown that PAX-loaded PNPs consisting of PCL-*b*-PEO copolymers prepared in gas-liquid microfluidic reactors showed slower drug release as Q increased, which we ascribed to shear-induced PCL crystallization within the core.[24, 27] PNPs consisting of MCL-containing copolymers were also found to exhibit a slowing of PAX release as the microfluidic flow rate increased, despite their relatively low core crystallinities compared to PCL.[30] Similar to that work, we attribute the flow-dependent increase in SN-38 release half times in Figure 7B to faster mixing times and more homogenously-distributed SN-38 within the PNP core. It is not clear why bulk-prepared PNPs show an intermediate release half time compared to the microfluidic values, although this may be a result of competing effects of slow water addition on the core crystallinity (which slows down release)[24, 27] and on interfacial SN-38 localization (which speeds up release).[30] The observed Q-dependent differences in release rates suggests that microfluidic shear processing could allow tuning of SN-38 pharmacokinetics *via* the manufacturing flow rate of microfluidic PNP formulations.

Cytotoxicity and Cell Uptake of SN-38-PNPs

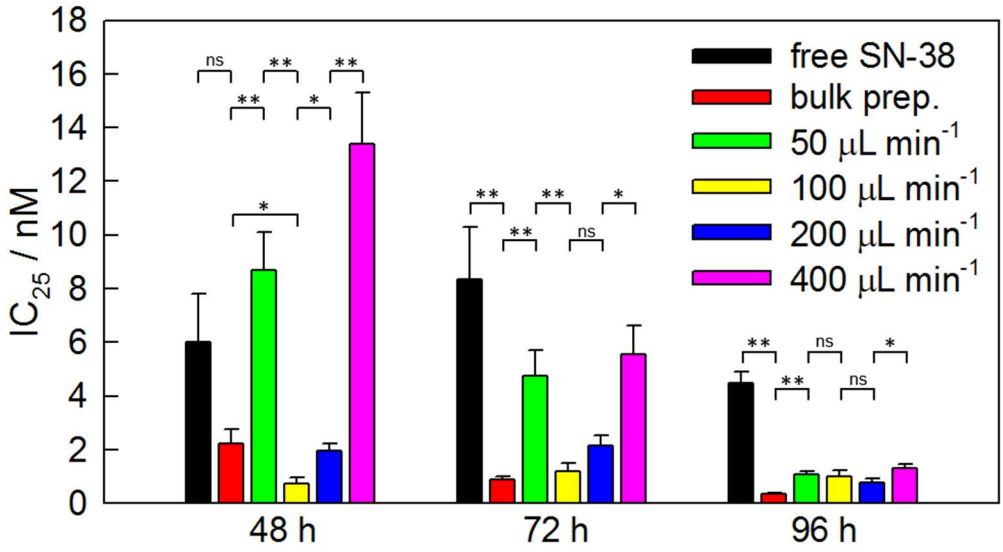

Figure 8. SN-38 potency against MCF-7 cells. Bar graph shows IC_{25} values for free SN-38 and SN-38-PNPs (r = 0.75) prepared using bulk and microfluidic (Q = 50, 100, 200, and 400 μL/min) methods. For each formulation method, IC_{25} values are shown for 48 h, 72 h, and 96 h incubation times. Labeled statistical comparisons indicate either no significant difference, $p > 0.05$ (ns) or significant difference, $p < 0.05$ (*) or $p < 0.005$ (**), between the various PNP formulations.

Microfluidic SN-38-PNPs (r = 0.75) prepared at four different flow rates (Q = 50, 100, 200, and 400 μL/min) along with the corresponding bulk-prepared sample were tested for cytotoxicity against the MCF-7 cell line with free SN-38 as a positive control. As reported in a previous publication, empty PNPs of PMCL-25 without drug showed no significant effect on MCF-7 cell viability: for polymer concentrations up to 36.5 ppm, negligible cell death was reported.[30] Since the highest polymer concentration applied in SN-38-PNPs doses in the current study was ~20 ppm, we conclude that SN-38 and not the excipient was responsible for observed cytotoxic effects. For free SN-38 and various SN-38-PNP formulations, cell death plots were generated for 48 h, 72 h, and 96 h incubation times (*Supporting Information*, Figures S3-S7). Since

SN-38 acts as a topoisomerase I inhibiter,[1] its inhibition activity does not lead to cell death significantly higher than 50% for some formulations. Therefore we chose to compare IC_{25} values (Figure 8) in addition to IC_{50} values (Figure S8). The IC_{50} results generally show higher experimental uncertainty than the corresponding IC_{25} values discussed below, although the resulting trends in both datasets were found to be consistent.

IC_{25} values (Figure 8) for microfluidic formulations were found to depend strongly on flow rate, indicating flow-tunable cytotoxic effects for SN-38-PNPs prepared in the gas-liquid reactor. For both 48 h and 72 h dosing times, IC_{25} values decreased sharply and then increased sharply as the manufacturing flow rate increased, with the lowest IC_{25} values and highest cytotoxic effects found for the intermediate Q = 100 and 200 μL/min flow rates. For the 48 h dosing time, the IC_{25} values of bulk-prepared SN-38-PNPs and free SN-38 are not significantly different. However, the Q = 100 μL/min microfluidic formulation shows a significantly lower IC_{25} value than either free SN-38 or bulk-prepared SN-38-PNPs. This suggests that flow-tunable, high-shear microfluidic manufacturing can produce SN-38-PNPs with stronger anticancer potencies than were achieved using a conventional bulk preparation under identical chemical conditions. For 72 and 96 h dosing times, we find that all PNP formulations show higher cytotoxicities (lower IC_{25} values) than those of free SN-38, suggesting that PNP encapsulation provides protection from conversion to the inactive carboxylate form leading to higher potencies over long exposure times. Interestingly, while SN-38-PNPs prepared at Q = 100 μL/min showed greater potency than the corresponding bulk-prepared PNPs after 48 h ($p < 0.05$), this difference was eroded at longer times. At 72 h there was no significant difference between bulk-prepared PNPs and SN-38-PNPs prepared at Q = 100 μL/min ($p > 0.05$), while at 96 h incubation, the bulk-prepared SN-38-PNPs displayed a greater

potency ($p < 0.05$). These data serve to highlight the subtle changes that can be accessed through different modes of encapsulation.

Comparing trends in 48-h and 72-h IC_{25} values of microfluidic SN-38-PNPs with respect to manufacturing flow rate to those of other properties (drug loading, size, and release rates), we find that cytotoxic effects most closely follow SN-38-PNP sizes as Q increases. Specifically, as $d_{h,eff}$ and $d_{h,N}$ values from DLS and d_{core} from TEM for the $r = 0.75$ series all reach their minimum values at the Q = 100 and 200 μL/min flow conditions (Figure 4), the corresponding IC_{25} values also reach a minimum (Figure 8). This suggests that flow tunable size *via* on-chip shear processing provides an experimental handle with which to modulate the *in vitro* potency of SN-38 nanomedicine formulations. The precise mechanism of this effect is currently unknown, although the combination of fewer large aggregates indicated by smaller $d_{h,eff}$ values (Figure 4A) and smaller nanoscale PNP sizes indicated by smaller $d_{h,N}$ and and d_{core} values (Figure 4B) are both expected to increase cellular uptake of SN-38-PNPs, which may explain the corresponding increased potency at intermediate flow rates.

Finally, we applied fluorescence imaging of MCF-7 cells in order to investigate cellular uptake of microfluidics-prepared DiI-labeled PNPs (DiI-PNPs). Compared to the SN-38-PNPs used in cytotoxicity experiments (Figure 8), the intensity-average mean effective hydrodynamic diameter of DiI-PNPs was about an order of magnitude smaller ($d_{h,eff}$ = 152 nm). This suggests an absence of large aggregates in DiI-PNPs which were found to be prevalent to varying degrees in SN-38-PNPs. However, the more pertinent size parameter with respect to cellular uptake is the number-average hydrodynamic parameter $d_{h,N}$, which for the SN-38-PNPs used to test cytotoxicity fell in the range of 15-36 nm, compared to a $d_{h,N}$ = 33 nm for DiI-PNPs. This indicates that the

DiI-labeled PNPs are a reasonable surrogate to confirm nanocarrier penetration into the cytosol of MCF-7 cells (Figure 9).

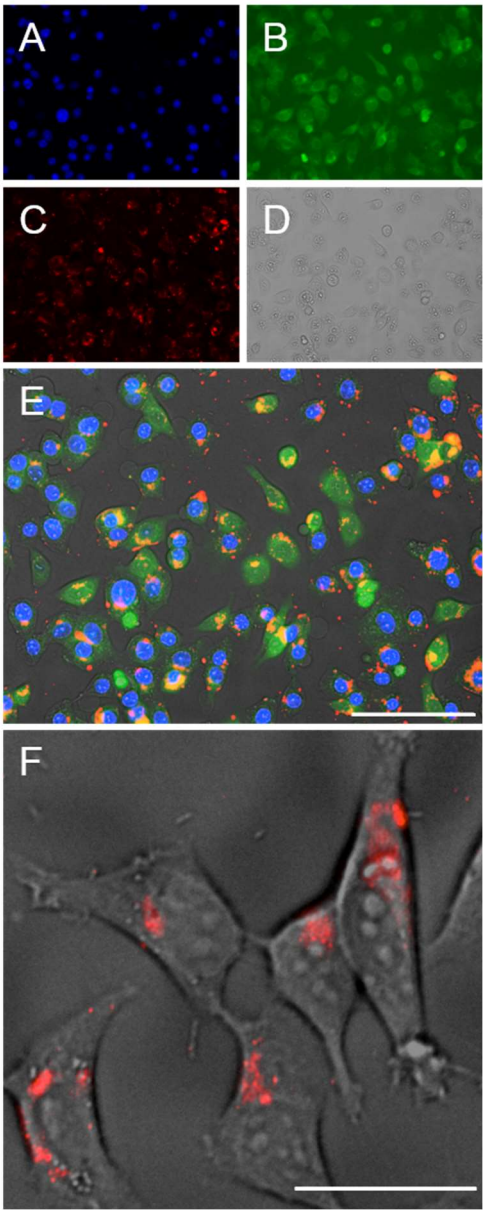

Figure 9. Fluorescent imaging data showing penetration of DiI-labeled PNPs (red) into MCF-7 cells. A–E: cells were counterstained with DAPI (blue) and fluorescein diacetate (green) to identify the nuclear and cytosolic compartments of the cells, and data was acquired using a 20× objective. (A) blue channel (DAPI), (B) green channel (fluorescein), (C) red channel (DiI), and (D) bright-field image. (E) Overlay of data from A–D showing particles localized mostly to the cytosolic regions of the cells. (F) A different population of cells treated with DiI-labeled PNPs and imaged

using a 60× objective; red channel is overlayed with the bright-field image, with red spots indicating DiI-labeled PNPs penetrating into the cytosol. Scale bars in E and F are 100 μm and 30 μm, respectively.

Conclusions

SN-38 is a potent and versatile anticancer agent for which PNP encapsulation can mitigate prohibitive instability and insolubility issues. New manufacturing approaches enabling continuous variation of the structure and properties of SN-38-PNPs without changes in the formulation chemistry offer obvious advantages for optimizing SN-38-based nanomedicines. Here we show that two-phase gas-liquid microfluidic reactors provide shear processing control of SN-38-PNPs through changes in manufacturing flow rate. Specifically, increasing the microfluidic flow rate (Q) led to nonmonotonic but consistent changes in encapsulation efficiency (EE) for various drug-to-polymer loading ratios (r). DLS and TEM analysis revealed a dominant population (by number) of nanosized particles (< 50 nm) along with a small number of larger aggregates (> 100 nm). As Q increased, the relative number and size of larger aggregates decreased through a minimum and then increased, attributed to a flow-variable competition of shear-induced particle breakup and shear-induced particle coalescence. At the same time, the size of nanosized particles also decreased through a minimum and then increased with increasing Q. SN-38 release half times were found to increase monotonically with increasing manufacturing flow rate on-chip, with microfluidic SN-38-PNPs prepared at high Q showing slower drug release than those prepared using a conventional bulk method. Interestingly, IC_{25} and IC_{50} values of the various SN-38-PNPs against MCF-7 showed strong flow rate dependencies that mirrored trends in particle size, with formulations showing both minimum particle sizes and maximum potencies produced at intermediate flow rates.

Importantly, the most potent microfluidic formulation showed a significantly lower IC_{25} value than the bulk-prepared SN-38-PNPs.

These results highlight the potential of microfluidic shear processing in two-phase reactors for providing more controlled manufacturing routes for optimizing new formulations and improving the properties of SN-38 nanomedicines. In addition, the comparison of these results to our previous study of PAX encapsulation under equivalent conditions underscores the general utility of microfluidic shear processing to manufacturing multiple therapeutic systems. However, it also shows that shear processing is not a "magic bullet" that produces the same results for every drug-polymer pair: formulation chemistry, and specifically the choice of encapsulated molecule, still play an important role in determining PNP structure and properties, even under conditions of strong and variable shear. Directed self-assembly is still self-assembly, and is therefore subject to intermolecular forces specific to each chemical system. This means that appropriate preliminary experimental work is required, in order to establish flow-dependent trends for different drugs and polymers on this microfluidic platform, before *a priori* "dial in" control of new nanomedicines can be established.

Supporting Information. TEM and DLS data for bulk-prepared SN-38-PNPs; additional SN-38 *in vitro* release profiles; complete MCF-7 cytotoxicity data for SN-38 and SN-38-PNPs; IC_{50} values for SN-38 and SN-38-PNPs; table of actual flow rates

Acknowledgements. We are grateful to the Natural Sciences and Engineering Research Council of Canada, NSERC, for financial support. We acknowledge Dr. Patrick Nahirney and the UVic EM lab (Department of Biology) for the continued use of their TEM.

References

1. Ebrahimnejad, P.; Dinarvand, R.; Sajadi, A.; Jaafari, M. R.; Nomani, A. R.; Azizi, E.; Rad-Malekshahi, M.; Atyabi, F., Preparation and in vitro evaluation of actively targetable nanoparticles for SN-38 delivery against HT-29 cell lines. *Nanomedicine: NBM* **2010,** *6*, 478-485.

2. Bala, V.; Rao, S.; Boyd, B. J.; Prestidge, C. A., Prodrug and nanomedicine approaches for the delivery of the camptothecin analogue SN38. *J. Control. Release* **2013,** *172*, 48-61.

3. Zhang, J. A.; Xuan, T.; Parmar, M.; Ma, L.; Ugwu, S.; Ali, S.; Ahmad, I., Development and characterization of a novel liposome-based formulation of SN-38. *Int. J. Pharmaceut.* **2004,** *270*, 93-107.

4. Roger, E.; Lagarce, F.; Benoit, J.-P., Development and characterization of a novel lipid nanocapsule formulation of Sn38 for oral administration. *Eur. J. Pharm. Biopharm.* **2011,** *79*, 181-188.

5. Hosseinzadeh, H.; Atyabi, F.; Varnamkhasti, B. S.; Hosseinzadeh, R.; Ostad, S. N.; Ghahremani, M. H.; Dinarvand, R., SN38 conjugated hyaluronic acid gold nanoparticles as a novel system against metastatic colon cancer cells. *Int. J. Pharmaceut.* **2017,** *526*, 339-352.

6. Peng, C.-L.; Lai, P.-S.; Lin, F.-H.; Wu, S. Y.-H.; Shieh, M.-J., Dual chemotherapy and photodynamic therapy in an HT-29 human colon cancer xenograft model using SN-38-loaded chlorin-core star block copolymer micelles. *Biomaterials* **2009,** *30*, 3614-3625.

7. Wei, X.; Gunatillake, P. A.; Moad, G.; Rizzardo, E.; Rosselgong, J.; Yang, W.; Thang, S. H., Synthesis of cleavable multi-functional mikto-arm star polymer by RAFT polymerization: example of an anti-cancer drug 7-ethyl-10-hydroxycamptothecin (SN-38) as functional moiety. *Sci. China Chem.* **2014,** *57*, 995-1001.

8. Matsumura, Y., Preclinical and clinical studies of NK012, an SN-38-incorporating polymeric micelles, which is designed based on EPR effect. *Adv. Drug Deliver. Rev.* **2011,** *63*, 184-192.

9. Koizumi, F.; Kitagawa, M.; Negishi, T.; Onda, T.; Matsumoto, S.-i.; Hamaguchi, T.; Matsumura, Y., Novel SN-38–incorporating polymeric micelles, NK012, eradicate vascular endothelial growth factor–secreting bulky tumors. *Cancer Res.* **2006,** *66*, 10048-10056.

10. Sumitomo, M.; Koizumi, F.; Asano, T.; Horiguchi, A.; Ito, K.; Asano, T.; Kakizoe, T.; Hayakawa, M.; Matsumura, Y., Novel SN-38–incorporated polymeric micelle, NK012, strongly suppresses renal cancer progression. *Cancer Res.* **2008,** *68*, 1631-1635.

11. Guo, Q.; Luo, P.; Luo, Y.; Du, F.; Lu, W.; Liu, S.; Huang, J.; Yu, J., Fabrication of biodegradable micelles with sheddable poly (ethylene glycol) shells as the carrier of 7-ethyl-10-hydroxy-camptothecin. *Colloid Surf. B* **2012,** *100*, 138-145.

12. Djurdjic, B.; Dimchevska, S.; Geskovski, N.; Petrusevska, M.; Gancheva, V.; Georgiev, G.; Petrov, P.; Goracinova, K., Synthesis and self-assembly of amphiphilic poly (acrylicacid)–poly (ε-caprolactone)–poly (acrylicacid) block copolymer as novel carrier for 7-ethyl-10-hydroxy camptothecin. *J. Biomater. Appl.* **2015,** *29*, 867-881.

13. Lee, S.-Y.; Yang, C.-Y.; Peng, C.-L.; Wei, M.-F.; Chen, K.-C.; Yao, C.-J.; Shieh, M.-J., A theranostic micelleplex co-delivering SN-38 and VEGF siRNA for colorectal cancer therapy. *Biomaterials* **2016,** *86*, 92-105.

14. Lu, L.; Zheng, Y.; Weng, S.; Zhu, W.; Chen, J.; Zhang, X.; Lee, R. J.; Yu, B.; Jia, H.; Qin, L., Complete regression of xenograft tumors using biodegradable mPEG-PLA-SN38 block copolymer micelles. *Colloid Surf. B* **2016,** *142*, 417-423.

15. Gan, M.; Zhang, W.; Wei, S.; Dang, H., The influence of mPEG-PCL and mPEG-PLGA on encapsulation efficiency and drug-loading of SN-38 NPs. *Artif. Cells Nanomed. Biotechnol.* **2017,** *45*, 389-397.

16. Dimchevska, S.; Geskovski, N.; Koliqi, R.; Matevska-Geskovska, N.; Vallejo, V. G.; Szczupak, B.; San Sebastian, E.; Llop, J.; Hristov, D. R.; Monopoli, M. P., Efficacy assessment of self-assembled PLGA-PEG-PLGA nanoparticles: Correlation of nano-bio interface interactions, biodistribution, internalization and gene expression studies. *Int. J. Pharmaceut.* **2017,** *533*, 389-401.

17. Rychahou, P.; Bae, Y.; Reichel, D.; Zaytseva, Y. Y.; Lee, E. Y.; Napier, D.; Weiss, H. L.; Roller, N.; Frohman, H.; Le, A.-T., Colorectal cancer lung metastasis treatment with polymer–drug nanoparticles. *J. Control. Release* **2018,** *275*, 85-91.

18. Schabas, G.; Wang, C. W.; Oskooei, A.; Yusuf, H.; Moffitt, M. G.; Sinton, D., Formation and shear-induced processing of quantum dot colloidal assemblies in a multiphase microfluidic chip. *Langmuir* **2008,** *24*, 10596-10603.

19. Wang, C. W.; Oskooei, A.; Sinton, D.; Moffitt, M. G., Controlled Self-Assembly of Quantum Dot-Block Copolymer Colloids in Multiphase Microfluidic Reactors. *Langmuir* **2010,** *26*, 716-723.

20. Wang, C. W.; Sinton, D.; Moffitt, M. G., Flow-Directed Block Copolymer Micelle Morphologies via Microfluidic Self-Assembly. *J. Am. Chem. Soc.* **2011,** *133*, 18853-18864.

21. Wang, C. W.; Bains, A.; Sinton, D.; Moffitt, M. G., Flow-Directed Assembly of Block Copolymer Vesicles in the Lab-on-a-Chip. *Langmuir* **2012,** *28*, 15756-15761.

22. Wang, C. W.; Bains, A.; Sinton, D.; Moffitt, M. G., Flow-Directed Loading of Block Copolymer Micelles with Hydrophobic Probes in a Gas-Liquid Microreactor. *Langmuir* **2013,** *29*, 8385-8394.

23. Wang, C. W.; Sinton, D.; Moffitt, M. G., Morphological Control via Chemical and Shear Forces in Block Copolymer Self-Assembly in the Lab-on-Chip. *ACS Nano* **2013,** *7*, 1424-1436.

24. Bains, A.; Cao, Y. M.; Moffitt, M. G., Multiscale Control of Hierarchical Structure in Crystalline Block Copolymer Nanoparticles Using Microfluidics. *Macromol. Rapid Comm.* **2015,** *36*, 2000-2005.

25. Bains, A.; Wulff, J. E.; Moffitt, M. G., Microfluidic synthesis of dye-loaded polycaprolactone-block-poly (ethylene oxide) nanoparticles: Insights into flow-directed loading and in vitro release for drug delivery. *J. Colloid Interf. Sci.* **2016,** *475*, 136-148.

26. Bains, A.; Moffitt, M. G., Effects of chemical and processing variables on paclitaxel-loaded polymer nanoparticles prepared using microfluidics. *J. Colloid Interf. Sci.* **2017,** *508*, 203-213.

27. Bains, A.; Cao, Y. M.; Kly, S.; Wulff, J. E.; Moffitt, M. G., Controlling structure and function of polymeric drug delivery nanoparticles using microfluidics. *Mol. Pharm.* **2017,** *14*, 2595–2606.

28. Xu, Z. Q.; Yan, B.; Riordon, J.; Zhao, Y.; Sinton, D.; Moffitt, M. G., Microfluidic Synthesis of Photoresponsive Spool-Like Block Copolymer Nanoparticles: Flow-Directed Formation and Light-Triggered Dissociation. *Chem. Mater.* **2015,** *27*, 8094-8104.

29. Xu, Z. Q.; Lu, C. H.; Riordon, J.; Sinton, D.; Moffitt, M. G., Microfluidic Manufacturing of Polymeric Nanoparticles: Comparing Flow Control of Multiscale Structure in Single-Phase Staggered Herringbone and Two-Phase Reactors. *Langmuir* **2016,** *32*, 12781-12789.

30. a. Xu, Z.; Lu, C.; Lindenberger, C.; Cao, Y.; Wulff, J. E.; Moffitt, M. G., Synthesis, Self-Assembly, and Drug Delivery Characteristics of Poly (methyl caprolactone-co-caprolactone)-b-poly (ethylene oxide) Copolymers with Variable Compositions of Hydrophobic Blocks: Combining Chemistry and Microfluidic Processing for Polymeric Nanomedicines. *ACS Omega* **2017,** *2*, 5289-5303; b. Xu, Z. Control of Structure and Function of Block Copolymer Nanoparticles Manufactured in Microfluidic Reactors: Towards Drug Delivery Appplications. M.Sc. Thesis, University of Victoria, Victoria, Canada (2016).

31. Ahmad, Z.; Shah, A.; Siddiq, M.; Kraatz, H. B., Polymeric micelles as drug delivery vehicles. *RCS Adv.* **2014,** *4*, 17028-17038.

32. Oltra, N. S.; Nair, P.; Discher, D. E., From Stealthy Polymersomes and Filomicelles to "Self" Peptide-Nanoparticles for Cancer Therapy. *Annu. Rev. Chem. Biomol.* **2014,** *5*, 281-299.

33. Letchford, K.; Liggins, R.; Wasan, K.; Burt, H., In vitro human plasma distribution of nanoparticulate paclitaxel is dependent on the physicochemical properties of poly(ethylene glycol)-block-poly(caprolactone) nanoparticles. *Eur. J. Pharm. Biopharm.* **2009,** *71*, 196-206.

34. Letchford, K.; Burt, H. M., Copolymer micelles and nanospheres with different in vitro stability demonstrate similar paclitaxel pharmacokinetics. *Mol. Pharm.* **2012,** *9*, 248-60.

35. Zhang, X.; Burt, H. M.; Hoff, D. V.; Dexter, D.; Mangold, G.; Degen, D.; Oktaba, A. M.; Hunter, W. L., An investigation of the antitumour activity and biodistribution of polymeric micellar paclitaxel. *Cancer Chemother. Pharmacol.* **1997,** *40*, 81-86.